The Planetary Science Journal, 2:39 (8pp), 2021 February https://doi.org/10.3847/PSJ/abd6e9
© 2021. The Author(s). Published by the American Astronomical Society.
OPEN ACCESS

Constraining the Positive Ion Composition in Saturn's Lower Ionosphere with the Effective Recombination Coefficient

Joshua Dreyer[1,2], Erik Vigren[1], Michiko Morooka[1], Jan-Erik Wahlund[1], Stephan C. Buchert[1], Fredrik L. Johansson[1,2], and Jack Hunter Waite[3]
[1] Swedish Institute of Space Physics, Uppsala, Sweden; joshua.dreyer@irfu.se
[2] Department of Physics and Astronomy, Uppsala University, Uppsala, Sweden
[3] Space Science and Engineering Division, Southwest Research Institute, San Antonio, USA
Received 2020 September 15; revised 2020 December 18; accepted 2020 December 24; published 2021 February 25

Abstract

The present study combines Radio and Plasma Wave Science/Langmuir Probe and Ion and Neutral Mass Spectrometer data from Cassini's last four orbits into Saturn's lower ionosphere to constrain the effective recombination coefficient α_{300} from measured number densities and electron temperatures at a reference electron temperature of 300 K. Previous studies have shown an influx of ring material causes a state of electron depletion due to grain charging, which will subsequently affect the ionospheric chemistry. The requirement to take grain charging into account limits the derivation of α_{300} to upper limits. Assuming photochemical equilibrium and using an established method to calculate the electron production rate, we derive upper limits for α_{300} of $\lesssim 3 \times 10^{-7}\,\mathrm{cm^3\,s^{-1}}$ for altitudes below 2000 km. This suggests that Saturn's ionospheric positive ions are dominated by species with low recombination rate coefficients like HCO^+. An ionosphere dominated by water group ions or complex hydrocarbons, as previously suggested, is incompatible with this result, as these species have recombination rate coefficients $> 5 \times 10^{-7}\,\mathrm{cm^3\,s^{-1}}$ at an electron temperature of 300 K.

Unified Astronomy Thesaurus concepts: Planetary science (1255); Saturn (1426); Space plasmas (1544); Recombination (2072)

1. Introduction

The joint NASA/ESA/ASI Cassini–Huygens mission surveyed the Kronian system in great detail after arriving at Saturn in 2004, providing unprecedented insight into the lower ionospheric altitudes during the so-called Grand Finale. In its final six orbits (288–293), Cassini dove to altitudes below $z < 2000$ km, where the bottom of the atmosphere ($z = 0$ km) by convention is placed at 1 bar atmospheric pressure. The onboard Radio and Plasma Wave Science (RPWS) instrument, including the Langmuir probe (LP), measured electron and total ion number densities (n_e and n_i), as well as electron temperatures (e.g., Wahlund et al. 2018; Hadid et al. 2019; Morooka et al. 2019). Number densities of H_2 and other neutral species, as well as light positive ions (H^+, H_2^+, H_3^+), were measured by the Ion and Neutral Mass Spectrometer (INMS; e.g., Waite et al. 2018).

The analysis of these data sets revealed a multitude of unexpected phenomena, such as prominent levels of electron depletion ($n_e \ll n_i$) at low altitudes. Assuming quasi-neutrality, a negatively charged dust component could act as the negative charge carrier alongside free electrons (Morooka et al. 2019). The nature of this dust component is not yet known. Its size distribution, composition, and origin remain to be detailed and this is outside of the scope of the present study. Similarly, observations of enhanced electron temperatures that seem to be related to the dusty plasma state in the deep ionosphere are yet to be explained (Morooka et al. 2019).

Original content from this work may be used under the terms of the Creative Commons Attribution 4.0 licence. Any further distribution of this work must maintain attribution to the author(s) and the title of the work, journal citation and DOI.

Early models of Saturn's ionosphere focused mainly on hydrogen chemistry, predicting a main ionosphere strongly dominated by H^+ (e.g., Capone et al. 1977). Subsequent radio occultation measurements from the Pioneer 11, Voyager 1 and 2 missions, and later also the Cassini mission (see, e.g., Nagy et al. 2006 and references therein) revealed peak electron number densities incompatible with (lower than) the early model predictions. It was realized that a mechanism is needed for converting atomic ions (particularly H^+) into molecular ions. The efficiency of any such mechanism is to be expected to reduce the number density of free electrons as the rate coefficient for dissociative recombination with molecular ions is some five orders of magnitudes higher than the rate coefficient for radiative association of electrons with atomic ions (see, e.g., Prasad & Huntress 1980). The main theories for the atomic to molecular conversion of ions are associated with vibrationally excited H_2 molecules and ring rain. As reviewed by Moore et al. (2004), when H_2 is in the fourth vibrational state or higher, the charge transfer reaction $H^+ + H_2 \rightarrow H + H_2^+$ can occur close to the collisional rate. The ring rain hypothesis (originally suggested by Connerney & Waite 1984) implies for instance that particles originating from Saturns rings can supply the ionosphere with molecules that are reactive with H^+ via charge transfer, for example H_2O. These two mechanisms may, of course, operate in parallel. To further illustrate the scientific progress over the past couple of decades, Moore et al. (2018) have reflected that nowadays the question has rather changed to why the observed amounts of H^+ are so unexpectedly high.

The dominating ion species at ionospheric altitudes below 2000 km are unknown. This is because of the high spacecraft velocity ($\sim 34\,\mathrm{km\,s^{-1}}$) and the ion optics design of INMS, which limited the number density retrievals to ions with mass-to-charge ratios less than ~8 Da. The main goal of the present study is to constrain the composition of the bulk positive ion

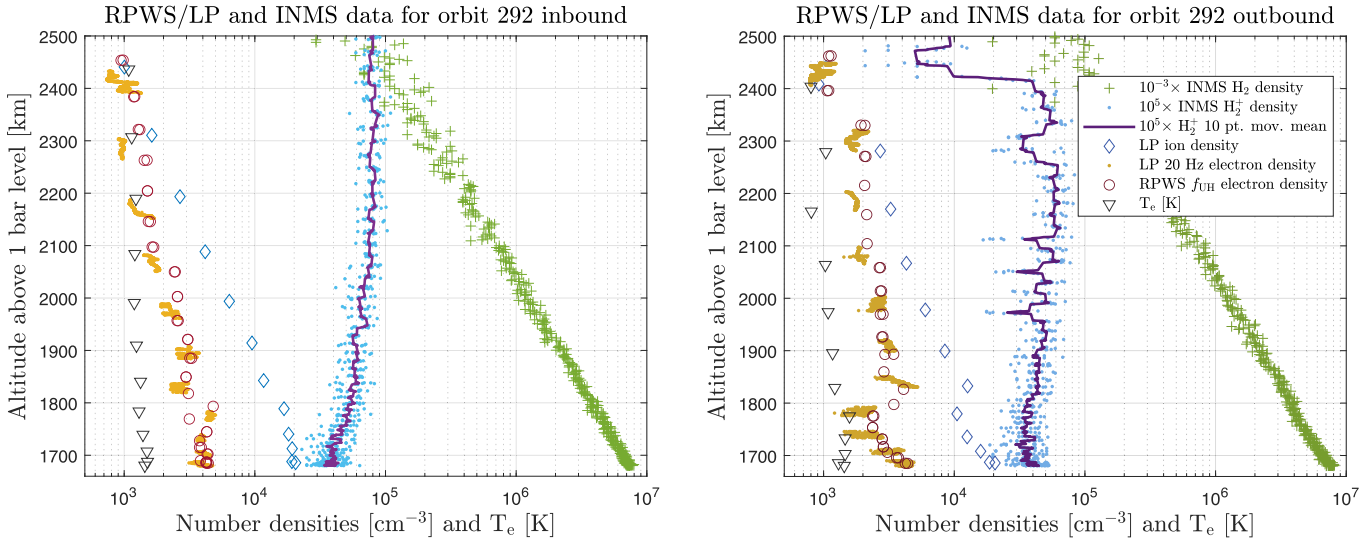

Figure 1. Plasma number densities in cm^{-3} and electron temperatures in Kelvin for orbit 292, with the inbound part of the orbit in the left and outbound in the right panel. H_2 and H_2^+ number densities are scaled down and up, respectively, to include in the same figure. A moving mean of the H_2^+ densities over 10 points is shown to aid with the identification of trends.

population in Saturns deep near equatorial ionosphere (our method does not provide any constraints on the nature of the negative ion population). This is done by combining RPWS/LP and INMS measurements to derive an upper limit of the effective recombination coefficient α_{300} at a reference electron temperature of 300 K. This upper limit is particularly helpful for ruling out the dominance of certain ion species which are known from laboratory measurements to have comparably high recombination rate coefficients. The present study focuses on equatorial latitudes, as the final orbits had their closest approaches around the equator. The relevant Cassini measurements are presented in Section 2, the chemical model used for this study in Section 3. Results are presented and discussed in Section 4. Finally, in Section 5 we summarize the work and provide some concluding remarks.

2. Cassini Data Set

A particular focus of this present study is on orbit 292, which is Cassini's final full orbit, with a periapsis of ∼1680 km on 2019 September 9 at 00:18 UTC. This orbit provided full high-quality RPWS and INMS data down to the lowest measured altitudes, which makes it particularly interesting for a detailed study of the ionospheric chemistry.

Orbit 288, with a periapsis of ∼1712 km on 2019 August 10 at 04:22 UTC, also has a full data set of INMS and RPWS/LP data. The data quality for this orbit is potentially less trustworthy, and seems to have been affected by a cloud of charged particles existing around the spacecraft (Morooka et al. 2019). This seemingly also applies to the LP sweep measurements around closest approach of orbit 289. As our analysis focuses on the lowest reached altitudes, these two orbits are not included in the present study.

The other orbits of the Grand Finale (290, 291, and 293) are missing H_2^+ INMS number density measurements. To extend the study to these orbits, we fit the H_2 measurements of orbit 292 to the H_2^+ measurements and can then derive H_2^+ number densities for the other orbits from their respective measured H_2 number densities (see Section 3.2). These are additionally corrected for variability in the solar extreme ultraviolet (EUV) spectrum using measurements from the Thermosphere Ionosphere Mesosphere Energetics and Dynamics Solar EUV Experiment (TIMED/SEE; see, e.g., Woods et al. 2005) extrapolated to Saturn's orbit.

2.1. RPWS/LP Measurements

We are using the ion number density measured by the LP, the electron number density derived from upper hybrid wave frequency measurements by the RPWS instrument, as well as electron temperatures from the LP in the calculations presented below. The RPWS instrument suite (including the LP), its operation, and the procedure to extract electron and ion number densities and temperatures from in situ measurements, are described in detail in Gurnett et al. (2004). The RPWS instrument typically measured whistler mode emissions, but these were heavily damped at the low altitudes during the Grand Finale orbits and instead a band propagating at the upper hybrid frequency f_{UH} was found (Persoon et al. 2019). This can be used to derive the electron plasma frequency from the upper hybrid frequency using $f_{UH}^2 = f_{pe}^2 + f_{ce}^2$, and thus the electron number density from the relation $f_{pe} = 8980\sqrt{n_e}$ Hz, with f_{pe} in Hz and n_e in cm^{-3} (Gurnett et al. 2004). In addition to these RPWS-derived electron number densities, they were also measured using both LP voltage sweeps and fixed voltage sampling at 20 Hz, with all three measurements agreeing typically within 10%–20%. In this study we use the electron number densities derived from the upper hybrid frequency band, as these provide consistent and rather evenly spaced (with respect to altitude) values, which makes them more suitable for interpolation.

Data for orbit 292 are shown in Figure 1. Probably the most notable fact about the electron and ion number densities is the strong depletion in the electron to ion number density ratio, starting at altitudes of around 2300 km and increasing at lower altitudes. This has been proposed to be a dust-related phenomenon by Morooka et al. (2019), who show that the electron depletion also seems to correlate with an increase in electron temperatures. A potential explanation is dust absorbing the electrons and taking over the role of negative charge carrier.

A slight increase in electron temperatures is visible at the lowest altitudes, contrary to model predictions with steadily decreasing temperatures toward the neutral temperatures at lower altitudes (e.g., Moore et al. 2008; Sakai & Watanabe 2016). Measurement results for the other analyzed orbits are shown in, for example, Morooka et al. (2019). As can be seen in their Figures 6 and 7, the n_e, n_i, and T_e altitude profiles are roughly similar for the inbound parts of orbits 290–293, though with exceptions of somewhat elevated values of n_i for orbit 290 and T_e in the case of orbit 293.

2.2. INMS Measurements

Ion and neutral number densities obtained from the INMS instrument, more specifically H_2 and H_2^+, are used in the following analysis. The INMS instrument, its operation, and the procedure to extract neutral and ion number densities from in situ measurements, are described in detail in Waite et al. (2004). For the analyzed orbits, the mass range of INMS is limited to ions with mass-to-charge ratios <8 Da.

The H_2 number densities measured during orbit 292 are shown in Figure 1, displaying a typical exponential increase toward lower altitudes. The H_2 number densities between the different proximal orbits are generally very similar, orbit 293 being the exception with lower overall H_2 number densities (which were measured at higher latitudes compared with the other orbits). H_2^+ number densities are expected to vary due to fluctuations in EUV flux and chemical processes. As they were only measured during orbit 292 of the analyzed set, differences between orbits are not directly obtainable. For orbit 292, H_2^+ number densities are generally between 0.3–1 cm^{-3} across the targeted altitude range below 2500 km. The sharp drop in densities for the outbound part at altitudes above 2400 km is a result of ring shadowing.

INMS measurement results for the other analyzed orbits are shown in, for example, Waite et al. (2018). Further discussion of the INMS data and its use in the present study can be found in Section 3.2.

3. Methods

In the following, we will provide a description of the chemical model used in the present study to derive an upper limit for the effective recombination coefficient α_{300} at a reference electron temperature of 300 K. This is essentially a weighted average of the recombination coefficients at 300 K of all present positive ion species. To reduce the impact of outliers on the required interpolation, the H_2 number densities are fitted. For orbits other than 292, H_2^+ number densities are unavailable and were fit-derived from orbit 292. A short overview of both fits is given in Section 3.2.

3.1. Photochemical Model Description

The continuity equation for the electron density in a dusty plasma, neglecting transport, can be written as

$$\frac{dn_e}{dt} = (P_{e,gas} + P_{e,dust}) - n_e(k_{DR}\, n_i + X_{dust}). \quad (1)$$

The electron production can be split into two terms, the production through photoionization of gas atoms or molecules ($P_{e,gas}$), and the production via photodetachment of electrons from dust grains ($P_{e,dust}$). Similarly, the loss rate can be split into a dissociative recombination loss term ($n_e\, k_{DR}\, n_i$, with the dissociative recombination rate coefficient k_{DR}) and one describing electron attachment to dust grains ($n_e X_{dust}$). The X_{dust} term corresponds to the effective electron attachment rate to dust grains, which depends for instance on the abundance of grains, their size- and charge distribution, and their shape, none of which are known. This may sound problematic, but when targeting an upper limit of α_{300}, X_{dust} is not necessary to determine. Below, we use $X_{dust,ion}$ in an equivalent manner for effective ion attachment to grains. At steady state, $dn_e/dt = 0$, yielding

$$P_{e,gas} + P_{e,dust} = n_e(k_{DR}\, n_i + X_{dust}). \quad (2)$$

Subtracting $P_{e,dust}$ from both sides gives

$$P_{e,gas} = n_e(k_{DR}\, n_i + X_{dust}) - P_{e,dust}. \quad (3)$$

The grain population absorbs free electrons and positive ions from the surrounding plasma, while losing electrons via photodetachment. At steady state these current contributions should balance:

$$n_e X_{dust} = P_{e,dust} + n_i\, X_{dust,ion}. \quad (4)$$

From this follows that $n_e\, X_{dust} > P_{e,dust}$, which in combination with Equation (3) leads to

$$P_{e,gas} > k_{DR}\, n_e\, n_i. \quad (5)$$

At this point, we have reached an inequality which is independent of X_{dust}. The dominant electron production process is the photoionization of H_2 leading to $H_2^+ + e^-$. As such the electron production rate is well approximated by the production rate of H_2^+. The production rate of H_2^+ is balanced by its loss rate, due primarily to the reaction $H_2^+ + H_2 \rightarrow H_3^+ + H$ which has a rate coefficient of $k_1 = 2 \times 10^{-9}\, cm^3\, s^{-1}$ (Theard & Huntress 1974). Combined, this gives the continuity equation for the H_2^+ density:

$$\frac{d[H_2^+]}{dt} = P_{e,gas} - k_1\, [H_2]\, [H_2^+]. \quad (6)$$

In equilibrium, the left side of the equation becomes zero, which enables us to determine $P_{e,gas}$ from the measured H_2 and H_2^+ number densities. The same approach for estimating the electron production rate has been applied in earlier studies (e.g., Moore et al. 2018; Cravens et al. 2019). It may be that the electron production rate is some 10%–15% higher than given by Equation (6) because electrons are also produced in the dissociative photoionization of H_2 leading to $H^+ + H + e^-$. The effect on our final results of taking into consideration this small relative increase is straightforwardly assessed.

The dissociative recombination of molecular ions is electron temperature dependent. The process is more efficient at lower electron temperatures and the dependence is usually in the form $(T_e/300\ K)^{-\beta}$, where T_e should be inserted in Kelvin, with β in the range 0.5–0.9 (see further Section 4). We utilize in this work the concept of an effective recombination and we set as default $\beta = 0.7$, similar to the choice made in the Titan ionospheric model of Vigren et al. (2013). Thus, as default for the dissociative recombination rate coefficient k_{DR}, we use

$$k_{DR} = \alpha_{300} \left(\frac{T_e}{300\text{K}}\right)^{-0.7}. \quad (7)$$

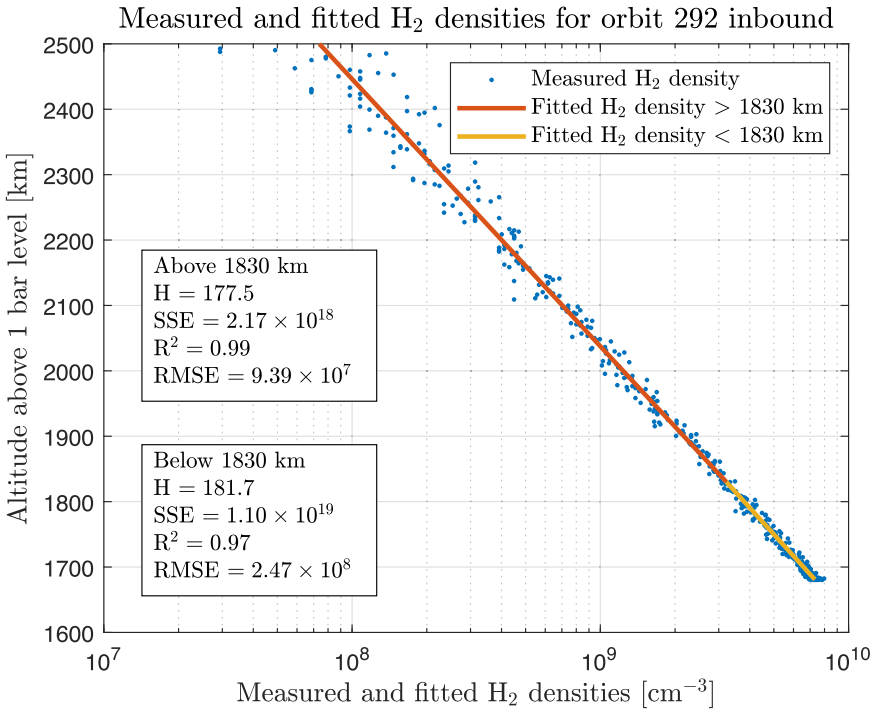

Figure 2. Comparison of H_2 number densities in cm^{-3} for the inbound part of orbit 292 with the derived fits, split into above and below 1830 km sections. The fit parameter H (denoting scale height) as described in Section 3.2 is displayed together with sum of squares due to error (SSE), R-square, and root mean squared error (RMSE) values.

Inserting this into Equation (5) and combining with Equation (6) in equilibrium yields

$$k_1\,[H_2]\,[H_2^+] > \alpha_{300}\left(\frac{T_e}{300\mathrm{K}}\right)^{-0.7} n_e\, n_i, \tag{8}$$

which, finally, can be rearranged to the following inequality for α_{300}:

$$\alpha_{300} < \frac{k_1\,[H_2]\,[H_2^+]}{n_e\, n_i}\left(\frac{T_e}{300\ \mathrm{K}}\right)^{0.7}. \tag{9}$$

To insert the different data sets into the equation, an interpolation at the measurement altitudes of the LP-derived total ion number density is made, due to these measurements being the sparsest. Assumed errors for this model are 10% for number density and temperature measurements (Morooka et al. 2019). We explore the range of uncertainties for the various measured parameters over 100,000 iterations, which yields a range of results, as shown in Section 4. Uncertainties in k_1 and β are not included in the error analysis, as these are deemed to be of systematic nature. Considering 15% errors in both k_1 and β implies an additional uncertainty of the α_{300} upper limits of up to $\sim 25\%$.

3.2. Fitted Data

Particularly at high altitudes, the measured H_2 number densities can vary substantially over minor altitude intervals. To limit the potentially large effect of these small-scale variations on the sparse interpolation used to derive upper limits for α_{300}, we fit a basic scale height exponential fit to the H_2 profiles. We find that a split fit with two different scale heights above and below 1830 km (1850 km for orbit 293) reproduces the measured data well. This particular split was found by testing various altitudes and comparing the fit qualities. An example for orbit 292 inbound is shown in Figure 2. The fit relates the measured H_2 densities to the respective altitudes (z) of the measurements: $[H_2] = n_0 \times \exp((z_0 - z)/H)$, with n_0 being the H_2 number density at the bottom end (z_0) of the column with a respective scale height H, which is the free parameter. The fit quality is very high for all orbits, with $R^2 > 0.95$ in all cases.

H_2^+ number densities were measured during orbit 292, but for orbits 290, 291, and 293 we are lacking these. To extend the study to include these orbits we derive the H_2^+ production rate from the measured data of orbit 292 inbound. This follows the form of an idealized Chapman profile: $[H_2^+] = a \times \exp(-b \times [H_{2,CD}])$, where a and b are best fit constants relating the measured H_2^+ concentration to the H_2 column density. The form of the fit function can be justified by the Beer–Lambert law. We assume that the intensity of the effective impinging ionizing radiation I relates to the column density $[H_{2,CD}]$ via an effective photoabsorption cross-section σ_{eff}: $I = I_0 \exp(-\sigma_{eff} / \cos(\theta_{SZA}) \times [H_{2,CD}])$, where I_0 is the unattenuated intensity and θ_{SZA} is the solar zenith angle ($\sim$22°–32° for 2500 km to closest approach). In our case the local production rate of H_2^+ is given by $P = I\,\sigma_{ion}\,[H_2]$, where σ_{ion} is the effective photoionization cross-section. The loss rate of H_2^+ is given by $L = k_1\,[H_2][H_2^+]$, so that in equilibrium $[H_2^+] = (I\ \sigma_{ion}/k_1) = (I_0\ \sigma_{ion}/k_1) \exp(-\sigma_{eff} / \cos(\theta_{SZA}) \times [H_{2,CD}])$. From this we can relate the fit parameters a and b to physical parameters. Combining solar EUV spectra from TIMED/SEE with photoionization and photoabsorption cross-sections for H_2 (Browning & Fryar 1973), we find theoretical values of a and b that differ from the best fit values: $a_{fit}/a_{theo} \approx 1.7$ and $b_{fit}/b_{theo} \approx 0.6$. The notable discrepancy for the a value is precisely in line with previous findings from observation/model comparisons by Moore et al. (2018). A contributing factor for this discrepancy could be the fact

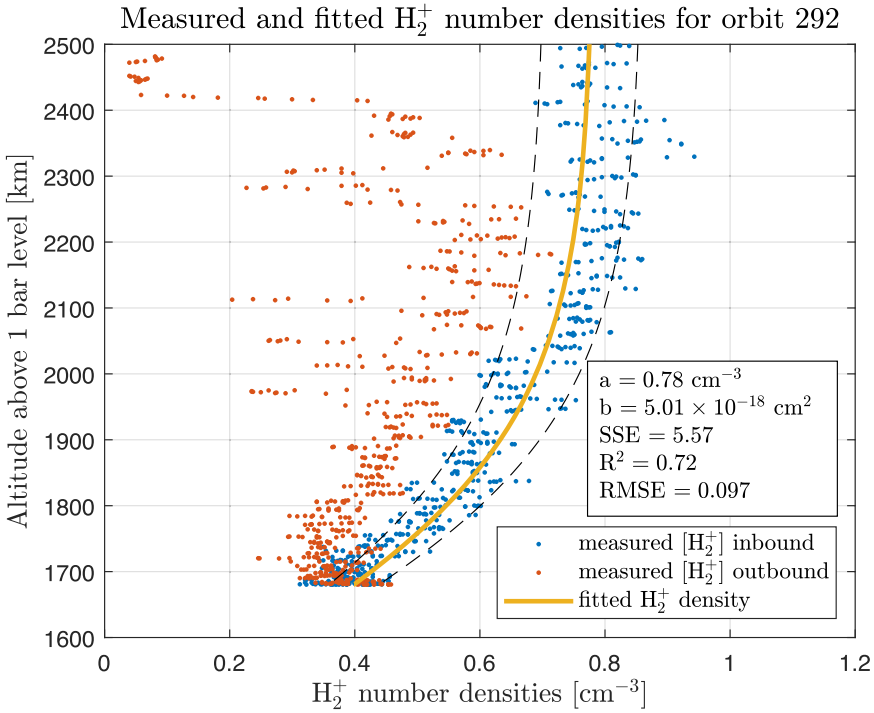

Figure 3. Comparison of H_2^+ number densities in cm^{-3} for the inbound and outbound parts of orbit 292 with the inbound-derived fit. The data was smoothed with a moving mean over five points to better illustrate trends, the fit itself is derived from the raw data. Black dashed lines indicate the ±10% fit error interval. Fit parameters as described in Section 3.2 are displayed together with sum of squares due to error (SSE), R-square, and root mean squared error (RMSE) values.

that we are neglecting photoelectron impact ionization. However, this effect is expected to be responsible for only up to ∼10% of the ionization for the altitudes considered here (Galand et al. 2009).

The fit-derived H_2^+ number densities below 2500 km are shown in Figure 3, together with the measured H_2^+ number densities (slightly smoothed with a moving mean over five values for visualization purposes) for orbit 292, split into in- and outbound parts. While idealized, the fit captures most of the measured data within a range of ∼10% (see dashed lines in Figure 3). Whereas the inbound number densities do not show any major trends outside of a decrease toward lower altitudes and some mildly fluctuating densities, the outbound part is characterized by pronounced dips in H_2^+ densities around 1980 km, 2050 km, 2110 km and 2300 km. Above 2400 km the ring shadowing clearly affects the densities, which drop to <0.1 cm^{-3}. The origin of the drops at lower altitudes is less clear (possibly a ringlet shadowing signature), and their presence makes using a similar fit function as for the inbound part problematic. We therefore chose not to fit the outbound H_2^+ number densities and only show the measurement-derived results for orbit 292.

The fit-derived H_2^+ number densities for orbits 290, 291, and 293 are ultimately corrected with the effective EUV flux discrepancy between orbit 292 and the respective orbit, that is to say the extrapolated TIMED/SEE EUV flux is convolved with photoionization cross-sections to calculate the effective difference in production rate. This should be the main factor in determining the H_2^+ production rate, and together with the measured H_2 number densities for each respective orbit as input, will likely result in the best estimate we can achieve for the other orbits.

4. Results and Discussion

The upper limits for α_{300} derived from measured data for orbit 292 are shown in Figure 4, split into the inbound and outbound parts. For the inbound part, the upper limits decrease from $\sim 4 \times 10^{-7}$ cm^3 s^{-1} at altitudes above 2000 km toward values around $\sim 2 \times 10^{-7}$ cm^3 s^{-1} at lower altitudes. The outbound part of the orbit shows a peak up to 4×10^{-7} cm^3 s^{-1} at altitudes below 1800 km and values below 2×10^{-7} cm^3 s^{-1} at higher altitudes. Median values of upper limits for α_{300} below 2500 km for the inbound and outbound part of orbit 292 are $(2.30 \pm 0.28) \times 10^{-7}$ cm^3 s^{-1} and $(1.87 \pm 0.24) \times 10^{-7}$ cm^3 s^{-1}, respectively.

The results for all analyzed orbits are visualized in Figure 5. For orbits 290, 291, and 293 we consider only the inbound parts and use modeled H_2^+ number densities, while all other data are measured by RPWS/LP or INMS. The inbound values at altitudes below 2000 km are mostly between (1–2) $\times 10^{-7}$ cm^3 s^{-1}, with a few outliers up to 3×10^{-7} cm^3 s^{-1}. The agreement between orbits with modeled H_2^+ number densities and 292 inbound is mostly good, except for significantly higher limits for the inbound part of orbit 292 at altitudes above 2000 km, with values around $\sim 4 \times 10^{-7}$ cm^3 s^{-1}. For altitudes below 2000 km and across all orbits shown in Figure 5, the median α_{300} value is $(1.93 \pm 0.25) \times 10^{-7}$ cm^3 s^{-1}.

The effective recombination coefficient reflects the relative abundance of different ion species, so variability in α_{300} should imply variability in the ion composition. However, when viewing Figures 4 and 5 it should be kept in mind that the variability in α_{300} may be smaller than what the figures tell at first glance because our method targets only the upper limits of α_{300}.

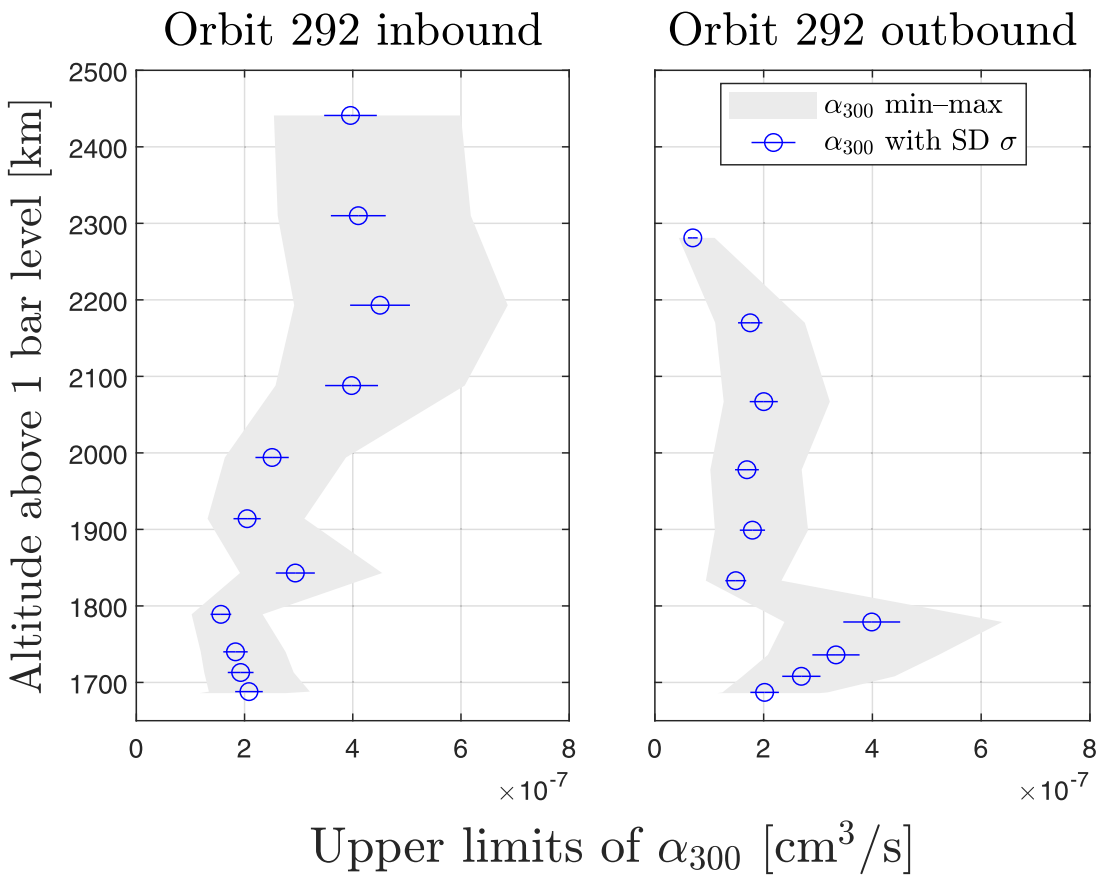

Figure 4. Derived upper limits for α_{300} for orbit 292, with the results for the inbound part of the orbit in the left and outbound in the right panel. Mean upper limit values are marked by a circle, with the standard deviation as a horizontal bar. The gray shaded area marks the extent of minimum and maximum calculated values from 100,000 iterations over the range of uncertainties for the various measured parameters.

The most striking variabilities in the upper limits of α_{300} are those mentioned above; the inbound–outbound asymmetry for 292 near closest approach, and for altitudes above 2000 km the markedly higher upper limits for the inbound part of orbit 292. In both cases the elevated limits are in a formal sense tied mainly to reduced electron densities (note for instance in Figure 1 the dip in the electron density profile near closest approach during the outbound of 292). If the assumption of photochemical equilibrium holds (discussed further below) and if the variability indeed reflects strong variations in the ion composition, we can at this point only speculate vaguely on causes, for example that there may be temporal variability and/or spatial asymmetries in the influx and sublimation of ring material. In the remaining discussion we shall instead focus on another conundrum, namely that the bulk of the derived upper limits of α_{300} are so low, particularly in the deep ionosphere where the assumption of photochemical equilibrium is to be expected the most robust (see Moore et al. 2004).

As mentioned in Section 3.1, the electron production rate may be underestimated by 10%–15% due to the additional production channel of $H_2 + \gamma \rightarrow H^+ + H + e^-$, which is it not included in the model. This would linearly increase the α_{300} upper limits by the same percentage. Still, the combined inbound data set suggests upper limits for the recombination coefficient of $\sim 2 \times 10^{-7}\,\mathrm{cm^3\,s^{-1}}$ around 1700 km altitude. For orbit 292, we have number density profiles of H^+ and H_3^+ (see, e.g., Figures 2 and 4 in Morooka et al. 2019). In the deep ionosphere they constitute a few to ~10% of the total ion number density as obtained from the LP measurements. The 300 K rate coefficients for the radiative recombination of H^+ and the dissociative recombination of H_3^+ are $\sim 3.5 \times 10^{-12}\,\mathrm{cm^3\,s^{-1}}$ (Prasad & Huntress 1980) and $1.15 \times 10^{-7}\,\mathrm{cm^3\,s^{-1}}$ (Sundström et al. 1994), respectively. The fractional abundances and rate constants of H^+ and H_3^+ can be included in the analysis to estimate an upper limit for the recombination coefficient characterizing the remaining ion population, α^*_{300}. Using this method yields a value of $\alpha^*_{300} \sim 2.4 \times 10^{-7}\,\mathrm{cm^3\,s^{-1}}$ around 1700 km. Unless the lower ionosphere is dominated by HCO^+, it is difficult to find an ion composition reconciling with this low upper limit of α^*_{300}, as will be detailed next.

In the recent study by Moore et al. (2018), ion compositions are calculated (see their Figure 2) based on a chemical model, a neutral background atmosphere constrained by INMS measurements (see Waite et al. 2018) and a few different assumptions as to what species (N_2, CO, C_2H_4) contributes the most to the 28 Da signal of the closed-source-mode INMS measurements. In all cases, H_3O^+, with a dissociative recombination rate coefficient of $7.6 \times 10^{-7}\,\mathrm{cm^3\,s^{-1}}$ (Neau et al. 2000), is predicted as the dominant ion for altitudes <1700 km. Our derived upper limit of $\alpha^*_{300} \sim 2.4 \times 10^{-7}\,\mathrm{cm^3\,s^{-1}}$ speaks against a deep ionosphere heavily dominated by H_3O^+. Furthermore, among the ions (excluding H^+ and H_3^+) predicted as the most abundant (H_3O^+, HCO^+, CH_3^+, CH_5^+, $C_2H_3^+$ and HCO_2^+) in the Moore et al. (2018) model only HCO^+, with $\alpha_{300} = 2 \times 10^{-7}\,\mathrm{cm^3\,s^{-1}}$ (Laubé et al. 1998), has a recombination rate coefficient less than $5 \times 10^{-7}\,\mathrm{cm^3\,s^{-1}}$ at 300 K (see Table 1). For the model using CO as the main contributor to the 28 Da signal, HCO^+ is predicted as the most abundant "heavy"

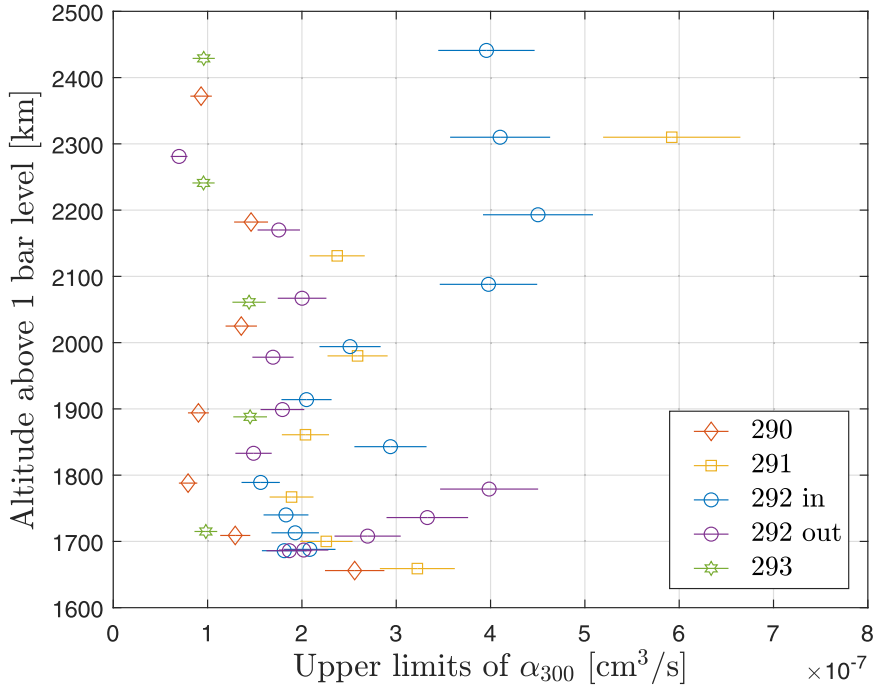

Figure 5. Derived upper limits of α_{300} for orbits 290–293 inbound, plus the outbound part of orbit 292. Mean upper limit values are marked by a shape for each orbit, with the standard deviation as a horizontal bar. Orbit 292 uses measured H_2^+ number densities, which are fit-derived for all other orbits.

Table 1
Rate Coefficients at an Electron Temperature of 300 K (α) and Electron Temperature Dependence (β) for Radiative or Dissociative Recombination of Indicated Ion Species

Ion	α [cm^3 s^{-1}]	β	Reference
H^+	3.5(−12)	0.75	Prasad & Huntress (1980)
H_3^+	1.2(−7)	0.65	Sundström et al. (1994)
H_3O^+	7.6(−7)	0.83	Neau et al. (2000)
HCO^+	2.0(−7)	0.79	Laubé et al. (1998), Hamberg et al. (2014)
HCO_2^+	1.2(−6)	0.64	Geppert et al. (2004b)
CH_3^+	7.0(−7)	0.61	Thomas et al. (2012)
CH_5^+	1.1(−6)	0.72	Kamińska et al. (2010)
$C_2H_3^+$	5.0(−7)	0.84	Kalhori et al. (2002)
N_2H^+	2.7(−7)	0.84	Vigren et al. (2012)
$C_2H_5^+$	1.2(−6)	0.79	McLain et al. (2004), Geppert et al. (2004a)
$HCNH^+$	2.8(−7)	0.65	Semaniak et al. (2001)
O_2^+	2.0(−7)	0.70	Alge et al. (1983)
NH_4^+	9.4(−7)	0.61	Öjekull et al. (2004)
$C_6H_7^+$	2.0(−6)	0.83	Hamberg et al. (2011)

Note. The rate coefficient at electron temperature T_e (in K) is given by $\alpha \times (T_e/300\,\mathrm{K})^{-\beta}$. Entries like 7.6(−7) are to be read as 7.6×10^{-7}. Ion species in bold are ones for which any of the models of Moore et al. (2018) predict concentrations exceeding 2×10^2 cm^{-3} around an altitude of 1700 km. Ion species in italic are examples of species not appearing in the model results displayed in Figure 2 of Moore et al. (2018).

ion (nonobservable by the INMS) species down to ∼1700 km, compared with much lower peak densities in the other modeled cases. Thus, the derived upper limits for α_{300} would suggest that CO is likely to be a major contributor to the 28 Da signal. In a recent analysis, Miller et al. (2020) suggest even higher fractional abundances of CO in the infalling ring material than reported by Waite et al. (2018), further strengthening this hypothesis. Generally, complex hydrocarbons and nitrile ions (with several C atoms) not included in the model have rate coefficients typically around 10^{-6} cm^3 s^{-1} (see Figure 6 in Vigren et al. 2013). Also, NH_4^+ is not included in the displayed model results by Moore et al. (2018). However, should NH_4^+ be among the dominant ions it would not aid in reducing the effective recombination coefficient, as it has a rate coefficient of 9.4×10^{-7} cm^3 s^{-1} (Öjekull et al. 2004). Examples (other than HCO^+) of molecular ions with rate coefficients closer to 2×10^{-7} cm^3 s^{-1} include, for example, O_2^+, N_2H^+ and $HCNH^+$, though neither of these latter ions are predicted to be dominant by Moore et al. (2018). Of the species shown in Table 1, a majority shows a temperature dependency exponent β between 0.6 and 0.8, which further justifies setting $\beta = 0.7$ for the determination of the effective recombination coefficient.

It would certainly be interesting to see how the output from a detailed chemical model, such as the one of Moore et al. (2018), would be affected by the incorporation of a dust component and equatorial ion transport. Models of Saturn's ionosphere have, to the best of our knowledge, not included dust charging or production of negative ions and as such worked with the assumption that the electron number density equals the total ion number density. Had we made this assumption in our analysis (and replaced $n_e\, n_i$ with n_e^2 in the denominator of Equation (9)), the median of the α_{300} upper limits below 2500 km would increase roughly by a factor of three and become more compatible with an ionosphere dominated by for instance H_3O^+. As detailed in Morooka et al. (2019), the LP sweeps have been checked against enhanced secondary electron emission possibly resulting from high velocity impacts on the probe. From that analysis it is unlikely that the ion densities used in the present study are markedly overestimated.

Plasma transport could in principle make the right-hand side of Equation (9) inapplicable (or at least questionable) as representative of an upper limit of α_{300}. Transport of charged dust could also violate our assumption that electrons locally attach to grains at a higher rate than they detach. This

assumption, critical for reaching the inequality relation given by Equation (5) (and indirectly also Equation (9)), seems however justified from the observations of increasing electron depletion levels at lower altitudes. The assumption of photochemical equilibrium below 2500 km is critical for our approach and justified only by previous investigations (e.g., Moore et al. 2004, 2018; Persoon et al. 2019). It is difficult to address the potential error of our upper limits should deviations from photochemical equilibrium be more severe than anticipated. Previous studies have assumed a dust-free plasma, whereas we now expect dust to play a significant role in Saturn's ionospheric chemistry. A higher concentration of dust might result in slower chemical loss, due to the resulting electron depletion. The precise effect on the PCE region is hard to assess, as the electron depletion is mostly observed toward the lowest altitudes that were reached by Cassini, where the chemical timescales are much shorter than the transport timescales. It is questionable whether the slower chemical loss due to dust chemistry would endanger the PCE assumption at these altitudes or whether there is enough dust present above 2000 km to shift the PCE limit. A reanalysis into this topic aided by the in situ measurements during the proximal orbits would certainly be of interest, but we refrain here from speculating on whether or not such a study would suggest a significant shift of the PCE limit.

5. Conclusion

In an attempt to constrain the positive ion composition in Saturn's ionosphere we targeted upper limits of the effective recombination coefficient using RPWS/LP and INMS measurements from Cassini's final four orbits. We derived, as presented and discussed above in Section 4, a median upper limit of α_{300} below 2000 km of $(1.93 \pm 0.25) \times 10^{-7}\,\mathrm{cm^3\,s^{-1}}$ (see Figure 5). In the deep ionosphere, the abundances of H^+ and H_3^+, both having low recombination coefficients, are small compared with the total ion density, and our analysis suggests that the remaining ion population then also should be characterized by a low effective recombination coefficient, for example $\sim 2.4 \times 10^{-7}\,\mathrm{cm^3\,s^{-1}}$ near an altitude of 1700 km. This indicates a positive ion population that is not dominated by water group ions or complex hydrocarbons, as these have 300 K recombination coefficients $> 5 \times 10^{-7}\,\mathrm{cm^3\,s^{-1}}$. The derived upper limits of α_{300} suggest an ion population dominated by ions with low effective recombination coefficients like $HCNH^+$ or HCO^+, the latter seeming more likely from the model predictions by Moore et al. (2018).

J.D. is thankful for being supported by the Swedish National Space Agency under grant Dnr 143/18. The research of F.L.J. was funded by the Swedish National Space Agency under grant Dnr 168/15. The Swedish National Space Board (SNSB) supports the RPWS/LP instrument on board Cassini.

ORCID iDs

Joshua Dreyer https://orcid.org/0000-0003-3038-3359
Erik Vigren https://orcid.org/0000-0003-2647-8259
Michiko Morooka https://orcid.org/0000-0001-9958-0241
Jan-Erik Wahlund https://orcid.org/0000-0002-2107-5859
Stephan C. Buchert https://orcid.org/0000-0003-2158-6074
Fredrik L. Johansson https://orcid.org/0000-0002-5386-8255
Jack Hunter Waite https://orcid.org/0000-0002-1978-1025

References

Alge, E., Adams, N. G., & Smith, D. 1983, JPhB, 16, 1433
Browning, R., & Fryar, J. 1973, JPhB, 6, 364
Capone, L. A., Whitten, R. C., Prasad, S. S., & Dubach, J. 1977, ApJ, 215, 977
Connerney, J. E. P., & Waite, J. H. 1984, Natur, 312, 136
Cravens, T. E., Moore, L., Waite, J. H., Jr., et al. 2019, GeoRL, 46, 6315
Galand, M., Moore, L., Charnay, B., Mueller-Wodarg, I., & Mendillo, M. 2009, JGRA, 114, A06313
Geppert, W., Ehlerding, A., Hellberg, F., et al. 2004a, PhRvL, 93, 153201
Geppert, W. D., Thomas, R., Ehlerding, A., et al. 2004b, FaDi, 127, 425
Gurnett, D. A., Kurth, W. S., Kirchner, D. L., et al. 2004, SSRv, 114, 395
Hadid, L. Z., Morooka, M. W., Wahlund, J.-E., et al. 2019, GeoRL, 46, 9362
Hamberg, M., Kashperka, I., Thomas, R. D., et al. 2014, JPCA, 118, 6034
Hamberg, M., Vigren, E., Thomas, R. D., et al. 2011, in EAS Pub. Ser. 46, PAHs and the Universe: A Symposium to Celebrate the 25th Anniversary of the PAH Hypothesis, ed. C. Joblin & A. G. G. M. Tielens (Les Ulis: EDP Sciences), 241
Kalhori, S., Viggiano, A. A., Arnold, S. T., et al. 2002, A&A, 391, 1159
Kamińska, M., Zhaunerchyk, V., Vigren, E., et al. 2010, PhRvA, 81, 062701
Laubé, S., Padellec, A. L., Sidko, O., et al. 1998, JPhB, 31, 2111
McLain, J. L., Poterya, V., Molek, C. D., Babcock, L. M., & Adams, N. G. 2004, JPCA, 108, 6704
Miller, K., Waite, J., Perryman, R., et al. 2020, Icar, 339, 113595
Moore, L., Cravens, T. E., Müller-Wodarg, I., et al. 2018, GeoRL, 45, 9398
Moore, L., Galand, M., Mueller-Wodarg, I., Yelle, R., & Mendillo, M. 2008, JGRA, 113, A10306
Moore, L., Mendillo, M., Müller-Wodarg, I., & Murr, D. 2004, Icar, 172, 503
Morooka, M. W., Wahlund, J.-E., Hadid, L. Z., et al. 2019, JGRA, 124, 1679
Nagy, A. F., Kliore, A. J., Marouf, E., et al. 2006, JGRA, 111, A06310
Neau, A., Al Khalili, A., Rosén, S., et al. 2000, JChPh, 113, 1762
Öjekull, J., Andersson, P. U., Någård, M. B., et al. 2004, JChPh, 120, 7391
Persoon, A. M., Kurth, W. S., Gurnett, D. A., et al. 2019, GeoRL, 46, 3061
Prasad, S. S., & Huntress, W. T., Jr. 1980, ApJS, 43, 1
Sakai, S., & Watanabe, S. 2016, Icar, 274, 261
Semaniak, J., Minaev, B. F., Derkatch, A. M., et al. 2001, ApJS, 135, 275
Sundström, G., Mowat, J. R., Danared, H., et al. 1994, Sci, 263, 785
Theard, L. P., & Huntress, W. T. 1974, JChPh, 60, 2840
Thomas, R. D., Kashperka, I., Vigren, E., et al. 2012, ApJ, 758, 55
Vigren, E., Galand, M., Yelle, R. V., et al. 2013, Icar, 223, 234
Vigren, E., Zhaunerchyk, V., Hamberg, M., et al. 2012, ApJ, 757, 34
Wahlund, J.-E., Morooka, M. W., Hadid, L. Z., et al. 2018, Sci, 359, 66
Waite, J. H., Lewis, W. S., Kasprzak, W. T., et al. 2004, SSRv, 114, 113
Waite, J. H., Perryman, R. S., Perry, M. E., et al. 2018, Sci, 362, aat2382
Woods, T. N., Eparvier, F. G., Bailey, S. M., et al. 2005, JGRA, 110, A01312